WARWICK
THE UNIVERSITY OF WARWICK

Manuscript version: Author's Accepted Manuscript
The version presented in WRAP is the author's accepted manuscript and may differ from the published version or Version of Record.

Persistent WRAP URL:
http://wrap.warwick.ac.uk/146910

How to cite:
Please refer to published version for the most recent bibliographic citation information. If a published version is known of, the repository item page linked to above, will contain details on accessing it.

Copyright and reuse:
The Warwick Research Archive Portal (WRAP) makes this work by researchers of the University of Warwick available open access under the following conditions.

© 2021 Elsevier. Licensed under the Creative Commons Attribution-NonCommercial-NoDerivatives 4.0 International http://creativecommons.org/licenses/by-nc-nd/4.0/.

Publisher's statement:
Please refer to the repository item page, publisher's statement section, for further information.

For more information, please contact the WRAP Team at: wrap@warwick.ac.uk.

warwick.ac.uk/lib-publications

Mode conversion of SH guided waves with symmetry inversion in plates

Alan C. Kubrusly[a], Pedro Tovar[a], Jean Pierre von der Weid[a], Steve Dixon[b]

[a]*Centre for Telecommunication Studies, Pontifical Catholic University of Rio de Janeiro, Rio de Janeiro, Brazil*
[b]*Department of Physics, University of Warwick, Coventry, CV4 7AL, UK*

Abstract

When shear horizontal ultrasonic guided waves interact with thickness discontinuities in plates, the reflected and transmitted wavefields can be composed of several modes due to mode conversion. It is known that in a plate with a symmetric discontinuity, with respect to the plate's mid-plane, mode conversion is restricted to modes that share the same symmetry as the incident mode. In this paper, we use an analytical model based on the reciprocity principle and finite element analysis to investigate mode conversion due to the interaction with different types of discontinuity, namely, non-symmetric, symmetric and geometrically symmetric but with opposite boundary conditions, that is one side of the discontinuity free and the other rigidly fixed. We show that the reflected field due to interaction with the latter is virtually restricted to modes with the opposite symmetry of the incident one, acting as a symmetry inverter discontinuity. Unlike fully symmetric discontinuities, the effectiveness of a symmetry inverter discontinuity depends on the frequency. This was proved with aid of the analytical model for a full-depth discontinuity and verified for partial depth discontinuities. Finally, symmetry inversion of SH waves was experimentally verified in acrylic plates which were symmetrically machined and filled with steel in one side to mimic a fixed boundary condition.

Keywords: SH guided waves, mode conversion, reciprocity principle, discontinuity, symmetry.

1. Introduction

Investigation of the interaction of Shear horizontal (SH) ultrasonic guided waves with discontinuities attracts attention since thickness discontinuities are commonly used to

Email addresses: alan@cpti.cetuc.puc-rio.br (Alan C. Kubrusly), S.M.Dixon@warwick.ac.uk (Steve Dixon)

model defects such as corrosion and cracks [1–3] and thus are relevant for non-destructive evaluation of plates and pipes [4, 5]. Depending on some parameters, such as the operating frequency-thickness product or the discontinuity shape, the interaction of SH waves with a discontinuity can be quite complex [6, 7]. Above the cut-off frequency of the first-order mode, the SH1 mode, when any SH guided wave mode impinges upon a discontinuity, the scattered field is potentially composed of several guided wave modes due to mode conversion [6–9], what renders interpretation of signals complicated.

The effect of a discontinuity on guided waves can be studied either experimentally [4, 6, 7, 10], numerically, using for instance finite element analysis [3, 8, 9], or analytically [1, 11–15]. The reciprocity theorem of elastodynamics relates the elastic solutions in two states within the same body [16] and can be used to analytically calculate the scattered field. This is accomplished by considering that one state consists of the response field in the presence of the discontinuity, whereas the other consists of a single-mode in the absence of the discontinuity. Pau et al. [11] used the reciprocity principle to calculate the reflected and transmitted field from discontinuities in a rod waveguide considering mode conversion. Recently, Lee et al. [12] used it to calculated the scattered field of the fundamental torsional mode in pipes from a more complex geometry, namely a tapered wall thinning, without, however, considering mode conversion. A similar analytical approach was used by Poddar and Giurgiutiu [13] to calculate the scattering coefficients of Lamb waves from thickness discontinuities by projecting the stress or displacement boundary conditions onto the, respectively, displacement or stress vector spaces of the guided wave modes, thus addressing projection in terms of the averaged power flow.

SH guided wave modes are classified between symmetric and antisymmetric according to their displacement profile across the plate's thickness. In principle, due to the incidence of a single SH mode upon a thickness discontinuity, any mode can arise due to mode conversion. However, if the discontinuity is symmetric with respect to the plate's centre, then only modes that share the same symmetry of the incident mode are reflected back or transmitted into the discontinuity. The reason for this lies in the symmetry of the boundary conditions that causes the solution to completely decouple between symmetric and antisymmetric modes. This phenomenon has been already verified either numerically

[8, 9, 17] or experimentally [17].

For a non-symmetric wall thinning, the values of the reflection coefficients depend on the thinning depth and edge angle. It has been observed that the reflection of a mode that has opposite symmetry as the incident one can be more intense than the reflection of the incident mode itself [6]. However, a complete symmetry inversion, that is, the reflected field being composed uniquely by modes with opposite symmetry as the incident mode, is a phenomenon that has not been observed.

This paper investigates whether, and under which conditions, an effective symmetry inversion arises. A previous preliminary study carried out with finite element analysis indicated that a geometrically symmetric discontinuity with opposite boundary conditions, meaning free on one side and rigidly fixed on the other, behaves as a symmetry inverter discontinuity [18]. Here, this phenomenon is verified and the study is comprehensively extended: the problem is analytically modelled by means of the reciprocity principle and also using commercial finite element software, the effectiveness of the symmetry inverter discontinuity as a function of the frequency is analysed and finally experimentally verified.

The rest of the paper is organized as follows. Section 2 derives the equations for the mode profiles and dispersion curves for SH waves in free-surface plates as well as in plates where one surface is free and the other is fixed. Section 3 exploits the reciprocity principle to solve the reflected and transmitted modes due to the interaction of an SH wave mode with discontinuities on either one or both surfaces of a plate where each side may be considered as free or fixed. Section 4 describes the finite element simulation setup. Section 5 shows the numerical and analytical results. Section 6 describe the experimental setup used to verify symmetry inversion and its results. Finally, section 7 concludes the work.

2. SH guided waves in plates

Shear horizontal (SH) guided waves [19] present only one non-null displacement component, in the z direction, perpendicular to the propagation direction, x, and to the coordinate of the plate thickness, y. The displacement field for an incident mode of order n is given by:

$$u_z(x, y, t) = A_n U_n(y) e^{j(\omega t - \kappa_n x)}, \tag{1}$$

where ω is the angular frequency, κ_n, A_n and $U_n(y)$ are the wavenumber, amplitude and displacement profile of mode n, respectively. The non-null stress components are:

$$\sigma_{xz} = \mu \frac{\partial u_z}{\partial x} = -j\mu\kappa_n A_n U_n(y) e^{j(\omega t - \kappa_n x)} \,, \tag{2a}$$

$$\sigma_{yz} = \mu \frac{\partial u_z}{\partial y} = \mu A_n \frac{\mathrm{d}U_n(y)}{\mathrm{d}y} e^{j(\omega t - \kappa_n x)} \,, \tag{2b}$$

where μ is the second Lamé constant of the medium. For SH waves, the equation of motion is:

$$c_T^2 \nabla^2 u_z = \ddot{u}_z \quad , \tag{3}$$

where the dot over a field means its time derivative, $c_T = \sqrt{\mu/\rho}$ is the shear speed of the medium, with ρ as the mass density. Applying Eq. 1 in Eq .3 yields

$$\frac{\mathrm{d}^2 U_n(y)}{\mathrm{d}^2 y} = -s^2 U_n(y) \tag{4}$$

where

$$s^2 = \left(\Omega^2 - \xi_n^2\right) \pi^2 / h^2 \quad , \tag{5}$$

with Ω and ξ_n being the adimensional frequency and wavenumber, given by

$$\Omega = \frac{\omega h}{\pi c_T} \quad , \tag{6a}$$

$$\xi_n = \frac{\kappa_n h}{\pi} \quad , \tag{6b}$$

and h is the plate thickness. The general solution of Eq.4 is

$$U_n(y) = C_n e^{+jsy} + D_n e^{-jsy} \quad , \tag{7}$$

where C_n and D_n are constants. The final expression for $U_n(y)$ and s are obtained by applying the boundary condition at the plate's surfaces.

2.1. SH guided waves in plates with free surfaces

The most common boundary conditions are both surfaces as free, i.e.:

$$\sigma_{yz}\Big|_{y=\pm h/2} = 0 \quad , \tag{8}$$

where the y coordinate is located at the middle of the plate. Using Eq.2(b) into Eq. 8 yields

$$C_n e^{\pm jsh/2} - D_n e^{\mp jsh/2} = 0 \quad , \tag{9}$$

whose solution is

$$sh = n\pi \quad , \tag{10}$$

and

$$C_n = D_n e^{jsh} \quad , \tag{11}$$

where n is an integer. Eq. 10 yields to the well-known dispersion relationship

$$\sqrt{\Omega^2 - \xi_n^2} = n \quad . \tag{12}$$

Solution is often expressed in terms of the phase speed, $c_n = \omega/\kappa_n$; the adimensional phase speed is

$$\eta_n = \frac{\Omega}{\xi_n} = \frac{c_n}{c_T} = \frac{\Omega}{\sqrt{\Omega^2 - n^2}} \quad . \tag{13}$$

Eq. 11 yields the modes' displacement profile:

$$U_n(y) = cos(n\pi y/h + n\pi/2)\,. \tag{14}$$

Figure 1(a) shows the displacement profile and Fig. 2 shows the phase speed dispersion curves for SH waves in a free-surface plate.

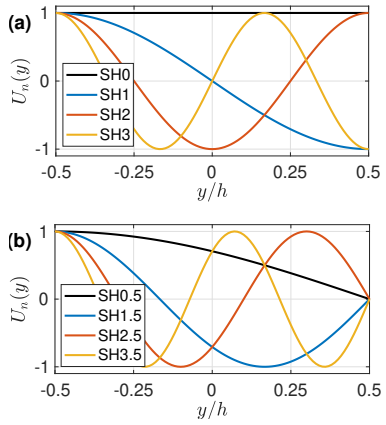

Figure 1: Displacement profile for SH guided wave modes in (a) free-surfaces plate, (b) free-fixed surfaces plate.

2.2. SH guided waves in plates with free-fixed surfaces

It is considered now that one of the surfaces is free and the opposite is fixed, for instance, the upper surface is fixed and the lower one is free. Then, the boundary conditions are:

$$\sigma_{yz}\Big|_{y=-h/2} = 0 \quad \text{and} \quad u_z|_{y=+h/2} = 0 \quad . \tag{15}$$

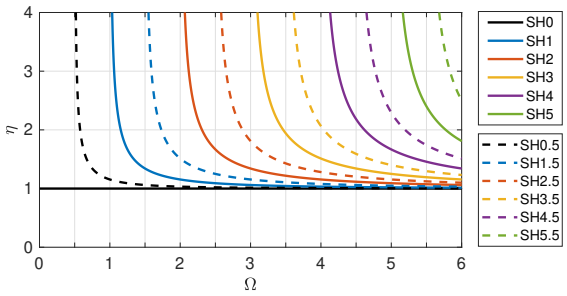

Figure 2: Phase speed of integer-order, continuous lines, and half-integer order, dashed line, SH guided wave modes. Half-integer modes propagate in a free-fixed plate.

Using Eq.2(b) and Eq.1 into Eq. 15 yields

$$\begin{cases} C_n e^{-jsh/2} - D_n e^{+jsh/2} = 0 \\ C_n e^{+jsh/2} + D_n e^{-jsh/2} = 0 \end{cases} . \tag{16}$$

The solution of Eq. 16 is

$$sh = \frac{2m+1}{2}\pi \quad , \tag{17}$$

where m is an integer. Setting $n = (2m+1)/2$, the same expression for the phase speed, Eq. 13, can be used but only half-integer order modes exits, i.e., $n = 0.5, 1.5, 2.5, 3.5...$. Eq. 11 and the expression for the modes' displacement profile, Eq.14, still hold with half-integer values for n. Figure 1(b) shows the displacement profile and Fig. 2 shows the phase speed dispersion curves for SH waves with half-integer order modes that propagate in a free-fixed surface plate.

SH modes in a free-surface plate are classified as symmetric and antisymmetric according to their displacement profile. Even-order modes are symmetric and odd-order modes antisymmetric. On the other hand, if the boundary conditions are free on one surface and fixed on the opposite surface, then modes are neither symmetric nor antisymmetric. Observing Eq.12 one can see that the mode n is propagating only if the Ω is above a cut-off value given by $\Omega_{\text{cut-off}} = n$, otherwise ξ_n is imaginary and mode n is evanescent, this is valid for either integer or half-integer modes.

2.3. Scattered field from a discontinuity

In this paper, it is considered a propagating SH wave mode in a free-surface plate that impinges upon a thickness discontinuity. This produces a reflected and transmitted fields that can be composed of several modes, due to mode-conversion, as follows:

$$u_r(x,y,t) = \sum_q R_{pq} A_p U_q^l(y) e^{j(\omega t + \kappa_q x)}, x < x_d \quad \text{and} \tag{18a}$$

$$u_t(x,y,t) = \sum_q T_{pq} A_p U_q^r(y) e^{j(\omega t - \kappa_q x)}, x > x_d \tag{18b}$$

where R_{pq} and T_{pq} are the reflection and transmission coefficients from incident mode p to scattered mode q and x_d is the longitudinal position of the discontinuity. The superscripts l and r mean that the mode's profile is taken at the left and right of the discontinuity, respectively. It is worth noting that for $U_q^r(y)$, the proper thickness at the right of the discontinuity has to be considered in Eq.14. Besides, depending on the boundary conditions at the right side of the discontinuity, one should assume integer or half-integer order transmitted modes.

The relevant stress component for calculating the scattered fields is σ_{xz}, given by Eq.2(a). The incident, reflected and transmitted σ_{xz} stress fields are, respectively:

$$\sigma_i(x,y,t) = -j\mu^l \kappa_p A_p U_p^l(y) e^{j(\omega t - \kappa_p x)}, x < x_d \tag{19a}$$

$$\sigma_r(x,y,t) = j\mu^l A_p \sum_q R_{pq} \kappa_q U_q^l(y) e^{j(\omega t + \kappa_q x)}, x < x_d \tag{19b}$$

$$\sigma_t(x,y,t) = -j\mu^r A_p \sum_q T_{pq} \kappa_q U_q^r(y) e^{j(\omega t - \kappa_q x)}, x > x_d\,. \tag{19c}$$

Therefore, the whole displacement and stress fields are, respectively:

$$u_z(x,y,t) = \begin{cases} u_i(x,y,t) + u_r(x,y,t) & , x < x_d \\ u_t(x,y,t) & , x > x_d \end{cases}, \tag{20}$$

$$\sigma_{xz}(x,y,t) = \begin{cases} \sigma_i(x,y,t) + \sigma_r(x,y,t) & , x < x_d \\ \sigma_t(x,y,t) & , x > x_d \end{cases}. \tag{21}$$

3. Analytical calculation of scattered modes

The reciprocity principle relates the elastodynamics of a body in two different states, namely A and B. Following Pau et al. [11] it can be written as:

$$\oiint_{\mathscr{S}} \left(\sigma_{ij}^{B} u_j^{A} - \sigma_{ij}^{A} u_j^{B}\right) n_i d\mathcal{S} = 0 \tag{22}$$

where, σ_{ij} is the stress tensor and u_j the displacement vector, superscripts A and B correspond to the state in which the fields are referred, $\mathscr{S}$ is a closed surface that encloses the volume of interest and n_i is the normal unit vector pointing outward $\mathscr{S}$. Implicit sum is considered for repeated indexes. In order to calculate the scattered field due to the interaction with a discontinuity, one should consider states A and B as the waveguide in the presence and absence of the discontinuity, respectively. Fig.3 illustrates both states and the surrounding surface $\mathscr{S}$.

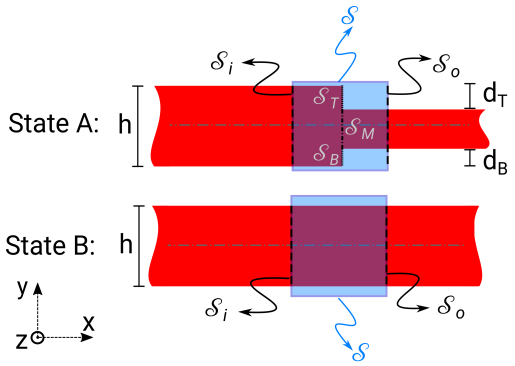

Figure 3: States A and B of a plate waveguide and coordinate system. State A represents the waveguide in the presence of a discontinuity, uniform along z with upper depth d_T and lower depth d_B. State B represents the waveguide in the absence of any discontinuity.

It is handy to consider that the input, $\mathscr{S}_i$, and output, $\mathscr{S}_o$, surfaces are both located at the discontinuity position. More precisely, at the left- and right-hand side limits of the discontinuity position, which, without loss of generality, can be chosen as $x_d = 0$. Thus, Eq. 22 reduces to:

$$-\iint_{\mathscr{S}_i} \left(\sigma_{xj}^{B} u_j^{A} - \sigma_{xj}^{A} u_j^{B}\right) d\mathcal{S} + \iint_{\mathscr{S}_o} \left(\sigma_{xj}^{B} u_j^{A} - \sigma_{xj}^{A} u_j^{B}\right) d\mathcal{S} = 0 \quad , \tag{23}$$

where the minus sign at the first term appears since the normal vector of $\mathscr{S}_i$ points leftwards. It is considered here that the discontinuity can be located at either the top, bottom or both sides, at the same longitudinal position. Then, $\mathscr{S}_o = \mathscr{S}_i = \mathscr{S}_\mathcal{B} \cup \mathscr{S}_M \cup \mathscr{S}_\mathcal{T}$, where $\mathscr{S}_\mathcal{B}$ and $\mathscr{S}_\mathcal{T}$ are free or fixed surfaces at the lower and upper parts of the discontinuity, respectively, and $\mathscr{S}_M$ is the middle surface, as illustrated in Fig.3. Thus, Eq.23 becomes

$$\begin{aligned} &-\iint_{\mathscr{S}_i}\left(\sigma_{xj}^{B}u_j^{A,l}-\sigma_{xj}^{A,l}u_j^{B}\right)d\mathcal{S}+\iint_{\mathscr{S}_\mathcal{B}}\left(\sigma_{xj}^{B}u_j^{A,l}-\sigma_{xj}^{A,l}u_j^{B}\right)d\mathcal{S}+\iint_{\mathscr{S}_\mathcal{T}}\left(\sigma_{xj}^{B}u_j^{A,l}-\sigma_{xj}^{A,l}u_j^{B}\right)d\mathcal{S}+ \\ &\iint_{\mathscr{S}_M}\left(\sigma_{xj}^{B}u_j^{A,r}-\sigma_{xj}^{A,r}u_j^{B}\right)d\mathcal{S}=0 \quad , \end{aligned} \tag{24}$$

where the second superscript, l or r, means to which part of the discontinuity state A is referred, either left or right-hand sides, respectively.

Here, $\sigma_{xj}^{A}=0$ or $u_j^{A}=0$ at $\mathscr{S}_\mathcal{B}$ or $\mathscr{S}_\mathcal{T}$, since each side of the discontinuity can be either free or fixed, respectively. Thus, letting $\mathcal{I}_\mathcal{B}=\iint_{\mathscr{S}_B}\left(\sigma_{xj}^{B}u_j^{A,l}-\sigma_{xj}^{A,l}u_j^{B}\right)d\mathcal{S}$ and $\mathcal{I}_\mathcal{T}=\iint_{\mathscr{S}_T}\left(\sigma_{xj}^{B}u_j^{A,l}-\sigma_{xj}^{A,l}u_j^{B}\right)d\mathcal{S}$, then

$$\mathcal{I}_{\mathcal{T},\mathcal{B}}=\begin{cases} \displaystyle\iint_{\mathscr{S}_{\mathcal{T},\mathcal{B}}}\sigma_{xj}^{B}u_j^{A,l}d\mathcal{S} & ,\ \mathscr{S}_{\mathcal{T},\mathcal{B}} \text{ is free} \quad (25a) \\ \displaystyle-\iint_{\mathscr{S}_{\mathcal{T},\mathcal{B}}}\sigma_{xj}^{A,l}u_j^{B}d\mathcal{S} & ,\ \mathscr{S}_{\mathcal{T},\mathcal{B}} \text{ is fixed} \quad . \quad (25b) \end{cases}$$

In order to evaluate Eq. 24, the displacement and stress fields at the left and righ-hand sides of the discontinuity, should be used for state A (given, for SH waves, by Eq.20 and Eq.21), whereas state B is composed by just one virtual mode, say m, that propagates in the waveguide in the absence of discontinuities. Evaluating Eq. 24 for incident mode p, considering N scattered modes and N modes as virtual waves, i.e., $0 \le q, m \le N-1$, yields:

$$\mathbf{\Gamma}\,\mathbf{R_p}+\mathbf{\Lambda}\mathbf{T_p}=\mathbf{f} \quad , \tag{26}$$

where $\mathbf{R_p}$ and $\mathbf{T_p}$ are column vectors of N elements containing the reflection and transmission coefficients, respectively, from mode p to each mode q, $\mathbf{\Gamma}$ and $\mathbf{\Lambda}$ are $N \times N$ matrices containing all terms related to the reflection and transmission, respectively and $\mathbf{f}$ is a column vector of N elements related only to the incident mode. Another set of equations

can be obtained by evaluating Eq.26 for the virtual mode m propagating in the negative direction. Organizing all equations in one single matrix leads to

$$\left[\begin{array}{c|c} \mathbf{\Gamma}^{+} & \mathbf{\Lambda}^{+} \\ \hline \mathbf{\Gamma}^{-} & \mathbf{\Lambda}^{-} \end{array}\right]\left(\begin{array}{c} \mathbf{R_p} \\ \hline \mathbf{T_p} \end{array}\right) = \left(\begin{array}{c} \mathbf{f}^{+} \\ \hline \mathbf{f}^{-} \end{array}\right), \tag{27}$$

where, the superscripts + and − means that the virtual mode m is propagating forwards or backwards, respectively. The reflection and transmission coefficients for the incident mode p is then obtained by solving Eq.27.

3.1. Free discontinuity

Consider, initially, the case in which both $\mathscr{S}_{\mathcal{T}}$ and $\mathscr{S}_{\mathcal{B}}$ are free. In this case, Eq. 24 is simplified by Eq. 25a as follows:

$$-\iint_{\mathscr{S}_M} \sigma_{xj}^{B} u_j^{A,l} d\mathcal{S} + \iint_{\mathscr{S}_i} \sigma_{xj}^{A,l} u_j^{B} d\mathcal{S} + \iint_{\mathscr{S}_M} \left(\sigma_{xj}^{B} u_j^{A,r} - \sigma_{xj}^{A,r} u_j^{B}\right) d\mathcal{S} = 0 \quad , \tag{28}$$

further applying Eqs.20 and 21 at $x = 0$ into Eq.28, dropping constants common to all terms and isolating terms that multiply the reflected, transmitted and incident modes, yields

$$\begin{aligned}
&\sum_q R_{pq}\left[\pm\kappa_m\mu^l \int_{-h/2+d_B}^{h/2-d_T} U_m^B(y)U_q^{A,l}(y)dy + \kappa_q\mu^l \int_{-h/2}^{h/2} U_q^{A,l}(y)U_m^B(y)dy\right] + \\
&\sum_q T_{pq}\left[\mp\kappa_m\mu^l \int_{-h/2+d_B}^{h/2-d_T} U_m^B(y)U_q^{A,r}(y)dy + \kappa_q\mu^r \int_{-h/2+d_B}^{h/2-d_T} U_q^{A,r}(y)U_m^B(y)dy\right] = \\
&\mp\kappa_m\mu^l \int_{-h/2+d_B}^{h/2-d_T} U_m^B(y)U_p^{A,l}(y)dy + \kappa_p\mu^l \int_{-h/2}^{h/2} U_p^{A,l}(y)U_m^B(y)dy \quad ,
\end{aligned} \tag{29}$$

where the plus-minus symbol, ±, means the sign which has to be taken when the virtual wave at state B is propagating forwards, upper symbol, and backwards, lower symbol. The integrals over $\mathscr{S}_i$ and $\mathscr{S}_M$ were replaced by integrals over y since the discontinuities are uniform along the width dimension, z, (see Fig.3).

The first bracket in Eq. 29 is $\Gamma_{qm}^{\pm}$, the second bracket is $\Lambda_{qm}^{\pm}$, and the right-hand side is $f_m^{\pm}$, being, respectively, the entries of the matrices $\mathbf{\Gamma}^{\pm}$, $\mathbf{\Lambda}^{\pm}$ and the vector $\mathbf{f}^{\pm}$. Eq.27 can be then evaluated and the reflection and transmission coefficients calculated.

3.2. Free-fixed discontinuity

If one of the discontinuity's surfaces is free and the opposite surface is fixed, for instance, $\mathscr{S}_{\mathcal{B}}$ is free and $\mathscr{S}_{\mathcal{T}}$ is fixed, then Eq. 24 becomes

$$-\iint\limits_{\mathscr{S}_M\cup\mathscr{S}_{\mathcal{T}}} \sigma_{xj}^{B}u_j^{A,l}d\mathcal{S}+\iint\limits_{\mathscr{S}_{\mathcal{B}}\cup\mathscr{S}_M} \sigma_{xj}^{A,l}u_j^{B}d\mathcal{S}+\iint\limits_{\mathscr{S}_M}\left(\sigma_{xj}^{B}u_j^{A,r}-\sigma_{xj}^{A,r}u_j^{B}\right)d\mathcal{S}=0 \quad , \tag{30}$$

and then,

$$\Gamma_{qm}^{\pm}=\pm\kappa_m\mu^l\int\limits_{-h/2+d_B}^{h/2}U_m^B(y)U_q^{A,l}(y)dy+\kappa_q\mu^l\int\limits_{-h/2}^{h/2-d_T}U_q^{A,l}(y)U_m^B(y)dy \tag{31a}$$

$$\Lambda_{qm}^{\pm}=\mp\kappa_m\mu^l\int\limits_{-h/2+d_B}^{h/2-d_T}U_m^B(y)U_q^{A,r}(y)dy+\kappa_q\mu^r\int\limits_{-h/2+d_B}^{h/2-d_T}U_q^{A,r}(y)U_m^B(y)dy \tag{31b}$$

$$f_m^{\pm}=\mp\kappa_m\mu^l\int\limits_{-h/2+d_B}^{h/2}U_m^B(y)U_p^{A,l}(y)dy+\kappa_p\mu^l\int\limits_{-h/2}^{h/2-d_T}U_p^{A,l}(y)U_m^B(y)dy \quad , \tag{31c}$$

It should be noticed that in this case, the discontinuity itself can be considered in two different ways. Namely, where just the vertical wall of the upper section of the discontinuity, $\mathscr{S}_{\mathcal{T}}$, is fixed or if the upper horizontal surface within the right-hand side of the discontinuity, namely $\{y = h/2 - d_T, x > 0\}$, is also fixed. Both types of fixed discontinuities are addressed by Eq.31. The difference lies in the type of the possible propagating modes at the right-hand side of the discontinuity. If only the upper vertical wall is fixed, then one should consider integer-order modes for $U_q^{A,r}(y)$, whereas if it has fixed boundaries all along the upper horizontal surface, then half-integer order should be used for $U_q^{A,r}(y)$.

3.3. Symmetric discontinuities

In this subsection it is discussed the particular case of geometrically symmetrical discontinuities, that is, when $d_T = d_B = d/2$. Two conditions are analyzed namely, both halves of the discontinuity are free, and when one half is free and the opposite is fixed.

For the former, a quick inspection of Eq. 29 reveals that, since all integrals have symmetric limits, then $\Gamma^{\pm}_{qm}$ and $\Lambda^{\pm}_{qm}$ nullify if mode m and q have the opposite symmetry, i.e., m is symmetric (even-order) and q is antisymmetric (odd-order) or vice versa. The same holds for $f^{\pm}_{m}$ with q replaced by p. Therefore, the system in Eq.27 is completely decoupled between symmetric and antisymmetric modes, and thus an incident symmetric (resp. antisymmetric) converts only to symmetric (resp. antisymmetric) modes. This was verified either numerically [8, 9] or experimentally [17].

For opposite boundary conditions, i.e. free-fixed, the analysis is far more complicated. First of all, if the fixed boundary condition extends along the right-hand side of the horizontal surface of the discontinuity, then transmitted modes are neither symmetric nor antisymmetric. Observing Eq.31 with $d_T = d_B = d/2$ there is no evident symmetry relationship that can be drawn. However, the particular case of an end reflection, i.e. $d_T = d_B = h/2$ is useful for gaining insight about how opposite boundary conditions act over a symmetric discontinuity. In this case, all transmitted coefficients vanish since there is no medium at the right of the discontinuity and only the forward propagating virtual wave at state B may be considered. Eq.27 is then simplified to $\mathbf{\Gamma}\,\mathbf{R_p} = \mathbf{f}$, where

$$\Gamma_{qm} = \kappa_m \mu^l \int_{0}^{h/2} U_m^B(y) U_q^{A,l}(y) dy + \kappa_q \mu^l \int_{-h/2}^{0} U_q^{A,l}(y) U_m^B(y) dy \tag{32a}$$

$$f_m = -\kappa_m \mu^l \int_{0}^{h/2} U_m^B(y) U_p^{A,l}(y) dy + \kappa_p \mu^l \int_{-h/2}^{0} U_p^{A,l}(y) U_m^B(y) dy \quad . \tag{32b}$$

Note that, if modes m and q in Eq.32a are both symmetric or both antisymmetric, then the argument of the integrals are even functions of y which implies

$$\int_{-h/2}^{0} U_q^{A,l}(y) U_m^B(y) dy = \int_{0}^{h/2} U_q^{A,l}(y) U_m^B(y) dy = \frac{1}{2} \int_{-h/2}^{h/2} U_q^{A,l}(y) U_m^B(y) dy \quad . \tag{33}$$

Due to modes orthogonality, the last term is non-zero only if m=q. If mode m is symmetric and q antisymmetric or vice versa, then the arguments of the integrals are odd functions

of y, consequently

$$\int_{-h/2}^{0} U_q^{A,l}(y) U_m^B(y) dy = -\int_{0}^{h/2} U_q^{A,l}(y) U_m^B(y) dy \quad . \tag{34}$$

Applying Eqs.33 and 34 into Eq.32, leads to

$$\Gamma_{qm} = \begin{cases} \mu^l \kappa_q \int_{-h/2}^{h/2} U_q^2(y) dy & , m = q \\ 0, & , m, q \text{ are both even or odd} \\ \mu^l (\kappa_m - \kappa_q) \int_{0}^{h/2} U_q^{A,l}(y) U_m^B(y) dy & , \text{otherwise} \end{cases} , \tag{35}$$

$$f_m = \begin{cases} 0, & , m, p \text{ are both even or odd} \\ -\mu^l (\kappa_m + \kappa_p) \int_{0}^{h/2} U_p^{A,l}(y) U_m^B(y) dy & , \text{otherwise} \end{cases} , \tag{36}$$

The latter shows that $\mathbf{f}$ has non-zero entries only corresponding to modes with opposite symmetry to the incident mode p. This condition applied to $\mathbf{\Gamma}\,\mathbf{R_p} = \mathbf{f}$ does not suffice to force the coefficient vector, $\mathbf{R_p}$, having non-zero entries uniquely to modes of the opposite symmetry as p, that is, a symmetry inverter discontinuity. Nevertheless, if $(\kappa_m - \kappa_q) \to 0$ then $\mathbf{\Gamma}$ is a diagonal matrix, and a symmetry inverter is achieved. Note that, the aforementioned condition occurs if $\Omega \to \infty$. This proves that a symmetric full-depth discontinuity with opposite boundary conditions inverts the symmetry of the incident mode at high-frequency. Partial-depth symmetric discontinuities with opposite boundary conditions are investigated in the next sections.

Here, three types of symmetric discontinuities are analysed plus a non-symmetric one. Fig.4 illustrates them, namely, (i) non-symmetric, (ii) symmetric, (iii) symmetric with one surface free and only the vertical wall of the opposite fixed, and (iv) symmetric with one surface free and the opposite fixed all along the right-hand side of the discontinuity. Discontinuity type (iii) has a less evident practical meaning. That is, when fixedly constraining the discontinuity, the most natural way of conceiving it, is by type (iv), namely,

on the vertical wall and along its extension than somehow restricting the fix boundary condition only to the vertical wall, like type (iii). Nevertheless, both types, (iii) and (iv), are considered here in order to allow comparison of the effect of integer and half-integer order modes propagating within the right-hand side of the discontinuity on the reflection and transmission coefficients, as shown in the next sections. Recall that either type (iii) or (iv) are solved by Eq.31, the difference being on which type of modes are considered for $U_q^{A,r}(y)$ in Eq.31b.

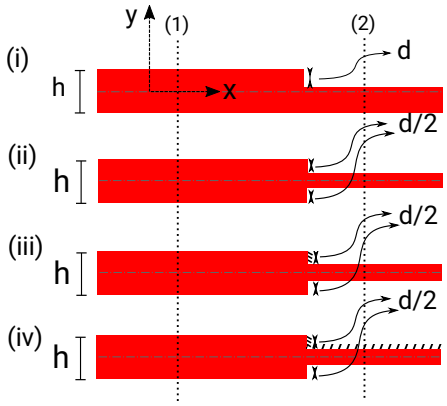

Figure 4: Types of discontinuities studied: (i) Non-symmetric, (ii) symmetric with both free surfaces, (iii) symmetric with one surface free and only the vertical wall of the opposite fixed (hatched area), and (iv) symmetric with one surface free and the opposite fixed (hatched area) all along thinner section. Within the numerical simulation, the origin is the position were generation occurs and (1) and (2) are receiving positions.

4. Finite Element Simulation of SH waves and discontinuities

Numerical analysis was also performed using a commercial time-domain Finite Element Method (FEM) solver, PZFlex©, which allows simulation of SH waves in a two-dimensional model. The four types of discontinuities shown in Fig.4 were modelled. In all cases, generation was imposed in the origin, at the left of the discontinuities. Receiving positions were set at the left and right of the discontinuity, represented by the vertical dotted lines (1) and (2) in Fig.4, in order to acquire reflected and transmitted waves. The material was modelled with shear wave speed $c_T = 3111\ m/s$ and plate thickness $h = 8mm$.

Generation was performed by imposing a force in the z-direction, modulated in time by an 8-cycle tone burst at 1000 kHz, thus, according to Eq.(6a), resulting in an adimensional frequency of $\Omega = 5.14$. The time-modulated force was applied to all nodes along the cross-section of the mesh, i.e. y-axis, following the displacement profile given by Eq. (14), according to the intended mode to be generated. Since modes' profiles form an orthogonal basis [17], this procedure ensures that only the mode that matches the applied profile is generated even at a high frequency-thickness.

Reception was performed by acquiring the response field along all nodes in the y-axis at either position (1) or (2). Also due to the modes' orthogonality, each SH mode n that composes the response field in Eq.(20) was extracted by integrating the product of the response field with $U_n(y)$, along the plate's thickness [20–22], through the following projection [17]:

$$u_n(x,t) = \frac{1}{C_n}\int_{-h/2}^{h/2} u(x,y,t)U_n(y)dy \quad , \tag{37}$$

such that $u_n(x,t)$ is the displacement field of mode n as a function of the longitudinal coordinate x and time and C_n is a constant defined by

$$C_n = \int_{-h/2}^{h/2} U_n(y)U_n(y)dy \quad . \tag{38}$$

It is worth noticing that Eqs.(37) and (38) hold for the left-hand side of the discontinuity. At the right-hand side of the discontinuity, one must change their integration limits to consider the thinner thickness. Also, for separating the modes transmitted to discontinuity type (iv), one has to consider the proper modes' profile of a free-fixed plate, i.e., $U_n(y)$ is given by Eq.14 with only half-integer order modes being allowed.

After the reflected and transmitted modes were separated, the peak-to-peak amplitude of the incident, reflected and transmitted modes were extracted in order to calculate the reflection and transmission coefficients:

$$R_{pq} = \frac{A_q^{(1)-}}{A_p^{(1)+}}, \tag{39a}$$

$$T_{pq} = \frac{A_q^{(2)+}}{A_p^{(1)+}}\sqrt{\frac{h-d}{h}} \quad , \tag{39b}$$

where $A_p^{(1)+}$, $A_q^{(1)-}$ and $A_q^{(2)+}$ are the peak-to-peak amplitude of the incident mode p, reflected mode q and transmitted mode q, respectively. Both incident and reflected waves were acquired at position (1) and were distinguished by their different times of arrival, whereas the transmitted wave was acquired at position (2). The square root in Eq.39b is included to compensate for the natural amplitude increase of a wave when it is transmitted into a thinner region of the plate.

5. Analytical and numerical results

The analytical model and numerical simulation were performed to investigate the interaction of SH guided wave with discontinuities types (i) to (iv), shown in Fig.4. In order to work in the high frequency-thickness regime, the operating adimensional frequency was set to $\Omega = 5.14$, both for finite element simulation and with the analytical model, so that modes SH0 to SH3 propagate with relatively low dispersion (see Fig.2) and thus the amplitude ratio of the simulated model can be straightly compared with the analytical coefficients. Fig.5 shows the reflection coefficients from each kind of discontinuity, where the discontinuity depth is $d/h = 0.5$ and the SH0 to SH3 modes were used as incident modes. Either analytical and numerical results are shown, where at each cell, the upper and lower triangles stand for numerical and analytical values, respectively.

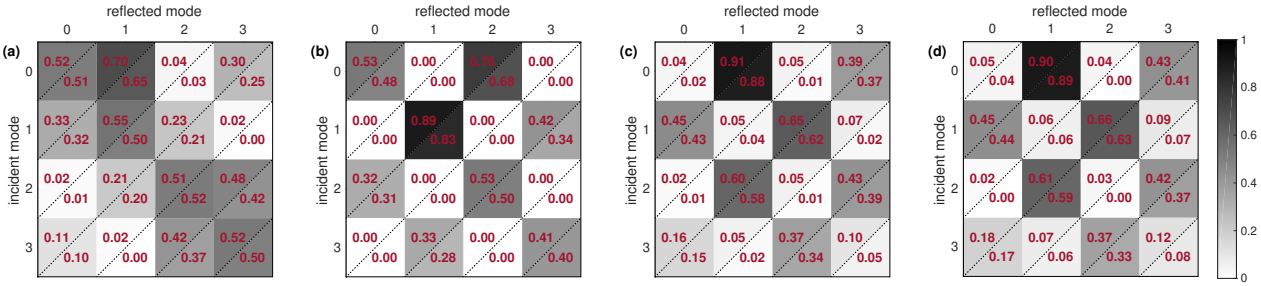

Figure 5: Reflection coefficients due to the interaction of SH guided wave modes with discontinuities types (i), (ii), (iii) and (iv), (a)-(d), respectively. The colourmap represents the intensity of the reflection coefficient. The numerical values of the reflection coefficients are shown in each cell. Upper and lower triangles represent numerical and analytical values, respectively.

With discontinuity type (i), a non-symmetric discontinuity, all modes can be converted due to the incidence of any mode. In a symmetric discontinuity, type (ii), the checkerboard

pattern in Fig.5(b) shows that there is conversion only to modes that share the same symmetry as the incident one, i.e., from an even (resp. odd) order mode, only even (resp. odd) order modes are created, as previously reported [17]. Fig.5(c) and (d) show the reflection coefficients for discontinuities types (iii) and (iv). Due to the opposite boundary condition on both surfaces of the plate (fixed and free), discontinuity type (iii) behaves virtually as a symmetry inverter. That is, when the incident mode is symmetric (resp. antisymmetric), the reflected modes are antisymmetric (resp. symmetric), as it can be seen from the reverse checkerboard pattern of Fig.5(c) and (d). It should be noticed that the values of converted modes with the same symmetry as the incident mode are very low, but are not zero. Also, reflection from discontinuities (iii) and (iv) are quite similar. In all cases, numerical and analytical results show very good agreement.

The reflection coefficients as a function of the discontinuity depth for discontinuities (i), (ii), (iii) and (iv) are shown in Fig.6(a) to (d), (e) to (h), (i) to (l) and (m) to (p), respectively. As it can be seen, from discontinuity (i) both symmetric and antisymmetric modes are converted, whereas with discontinuity type (ii), mode symmetry is preserved for any defect depth. Discontinuities with free-fixed surfaces, (iii) and (iv), strongly reflect modes with opposite symmetry, showing low-amplitude, same-symmetry modes for all depths. Interestingly, discontinuity (iii) and (iv) show very similar behaviour, except for very shallow discontinuities. This happens because, a zero-depth discontinuity of type (iv) means that at the right of the discontinuity the plate has the same thickness, but one of the surfaces is fixed. Thus, there is a change on the boundary conditions forcing reflection, as can be seen in Fig.6(i) to (l). On the other hand, a zero-depth type (iii) discontinuity means absolutely no change and, therefore, there is no reflected mode whatsoever, as is for discontinuity (ii).

Fig.7 shows the transmission coefficients from discontinuities of type (i), (ii), (iii) and (iv) for $d/h = 0.5$. Conversion to transmitted mode SH3 is not shown since it is evanescent at the discontinuity depth. The square root term in the transmission coefficient, see Eq.39b, is included in either numerical and analytical coefficients. As it can be seen, all modes are possible to be converted in case (i). Case (ii) shows the same checkerboard patters as observed with the reflection coefficient. Unlike for the reflection coefficient, cases

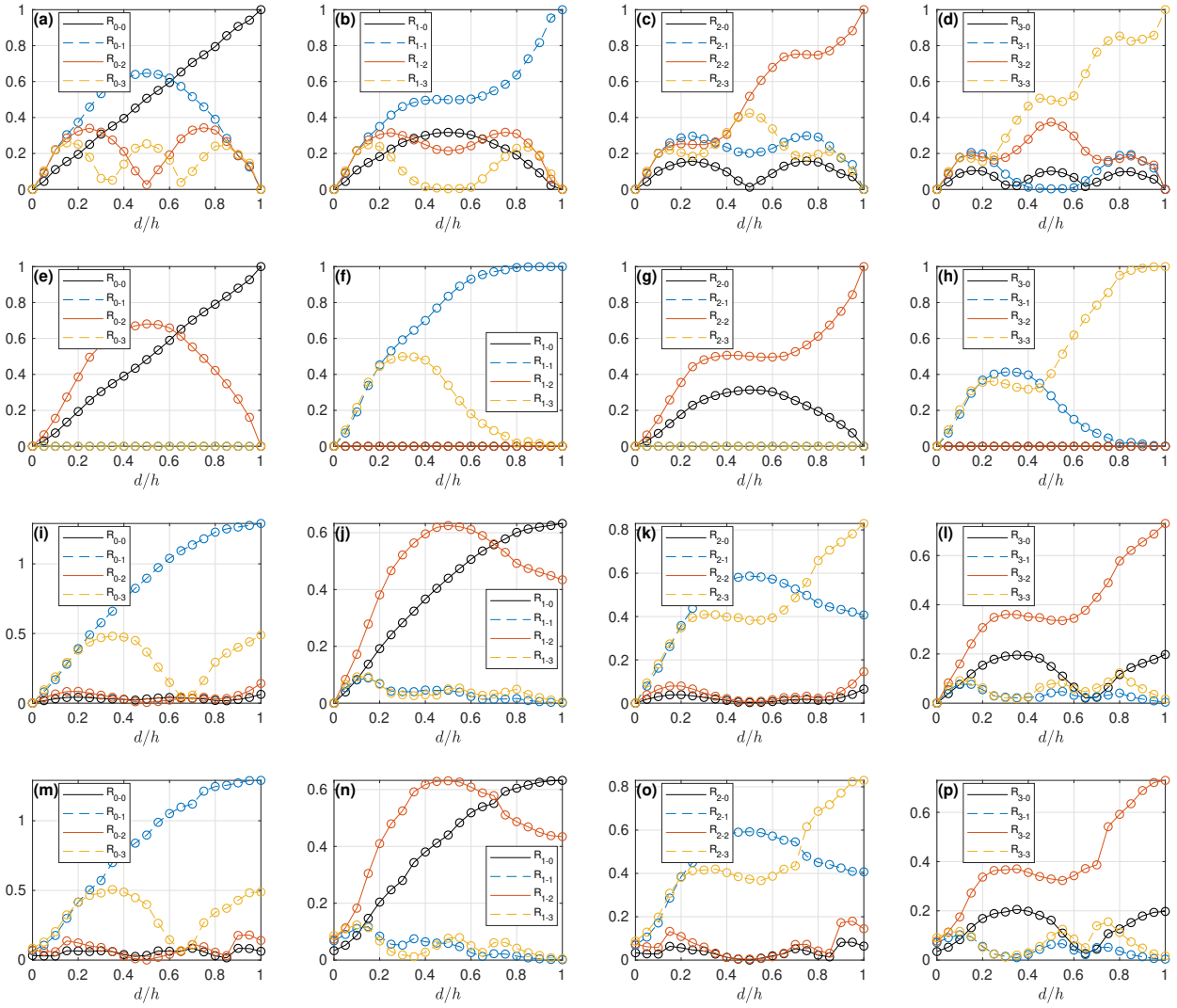

Figure 6: Analytically calculated reflection coefficients as a function of the discontinuity depth for discontinuities types (i), (a)-(d), (ii), (e)-(f), (iii), (i)-(l), and (iv), (m)-(p).

(iii) and (iv) behave differently, since case (iv) supports only half-integer order modes as transmitted modes. Conversion to higher-order, that is, SH2 and SH2.5, show lower agreement between numerical and analytical coefficients. This is because, these modes at half of the plate's thickness, i.e., at $\Omega = 2.57$, are very dispersive, mainly SH2.5, as can be seen in Fig.2. Thus, the pulse is significantly spread, altering its amplitude.

Fig.8 shows the transmission coefficient as a function of the discontinuity depth. Discontinuity type (ii) restricts mode conversion preserving symmetry, as happens for the reflection coefficient. Unlike for the reflection coefficient, symmetry inversion does not

happen for transmission to discontinuity (iii) and it makes no sense in discontinuity (iv) since symmetry classification for transmitted modes does not hold.

5.1. *Frequency analysis*

As discussed in section 3.3, a symmetric discontinuity with both free surfaces restricts mode conversion, preserving the symmetry of incident modes, whereas a symmetric discontinuity with opposite free-fixed surfaces tends to reflect modes with the inverse symmetry to the incident mode for high-frequencies. This is assessed here with the aid of the analytical model. Fig.9 shows the reflection coefficient for the first four SH modes for several adimensional frequencies. As it can be seen, the higher Ω, the more clear the inverse checkerboard pattern is.

Further quantitative analysis was carried out by calculating the same to opposite symmetry ratio (*SOSR*). This is defined as the sum of the squared reflection coefficients of modes with the same symmetry as the incident one per the sum of the squared reflection coefficients of modes with opposite symmetry as the incident one:

$$SOSR = \frac{\sum\limits_{\substack{p,q \text{ even} \\ \cup \\ p,q \text{ odd}}} |R_{pq}|^2}{\sum\limits_{\substack{p \text{ even},\, q \text{ odd} \\ \cup \\ p \text{ odd},\, q \text{ even}}} |R_{pq}|^2} \quad . \tag{40}$$

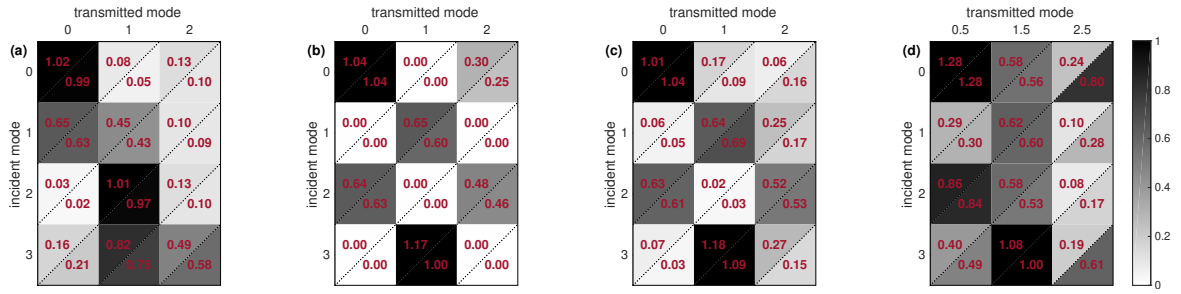

Figure 7: Transmission coefficients due to the interaction of SH guided wave modes with discontinuities types (i), (ii), (iii) and (iv), (a)-(d), respectively. The colourmap represents the intensity of the reflection coefficient. The numerical values of the reflection coefficients are shown in each cell. Upper and lower triangles represent numerical and analytical values, respectively.

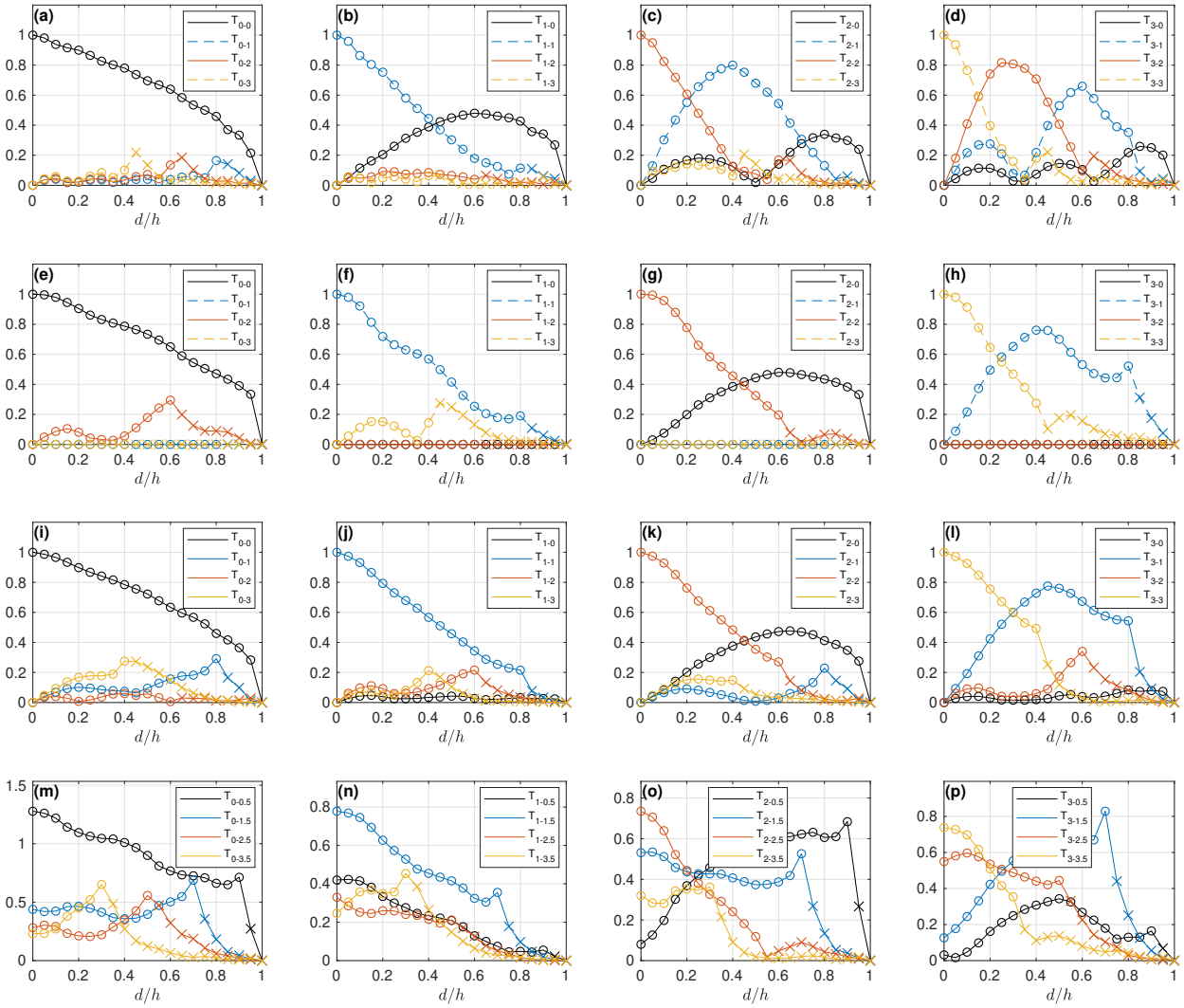

Figure 8: Analytically calculated transmission coefficients due to the interaction of SH guided wave modes with discontinuities types (i), (a)-(d), (ii), (e)-(f), (iii), (i)-(l), and (iv), (m)-(p). Crosses mean that the mode is evanescent at the discontinuity thickness.

SOSR as a function of Ω is shown in Fig.10 for a half-thickness and full-thickness discontinuities. As it can be seen, the higher the frequency, the lower *SOSR*. Therefore, further confirming that a symmetric discontinuity with opposite free-fixed boundary conditions behaves as a symmetry inverter discontinuity at high-frequency even from non-full depth discontinuities.

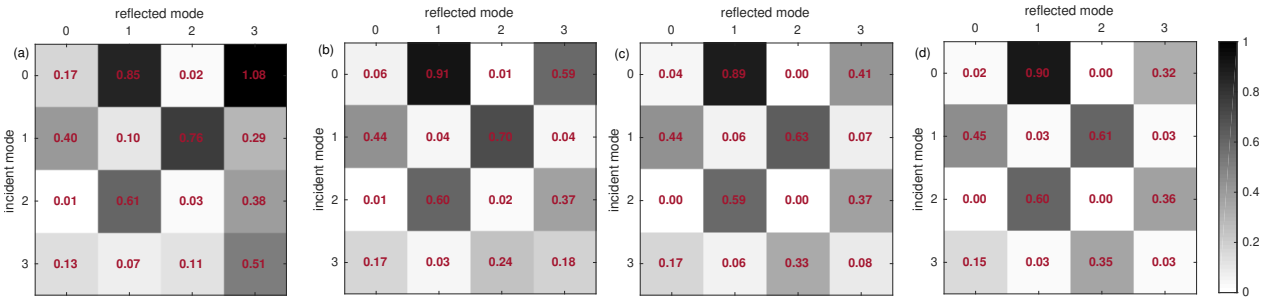

Figure 9: Reflection coefficients from discontinuities types (iv) with $d/h = 0.5$ at Ω equal to 3.1 (a), 3.6 (b), 5.1 (c) and 10.3 (d) obtained with analytic model.

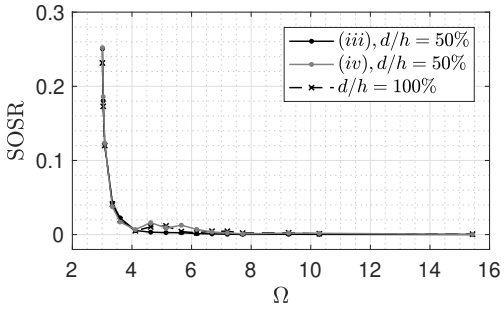

Figure 10: Same to opposite symmetry ratio, SOSR, of converted modes from discontinuities types (iii) and (iv) as a function of frequency. Types (iii) at $d/h = 0.5$, dot markers and black lines, types (iv) at $d/h = 0.5$, dot markers and grey lines, and $d/h = 1$, cross markers.

6. Experimental validation

6.1. Experimental setup

It has been shown previously [18] that a fixed boundary condition can be effectively approximated by an interface with a high acoustic impedance material. Accordingly, an experimental setup has been designed to verify mode conversion with symmetry inversion. Acrylic plates were used in which symmetric discontinuities were machined. In order to simulate a fixed boundary condition on the symmetric discontinuity, a steel plate was used to fill all the machined depth. Considering the nominal density and transverse wave speed of acrylic as $\rho = 1180\,kg/m^3$ and $c_T = 1373\,m/s$, and of steel as $7800 kg/m^3$ and $3200\,m/s$, the respective shear acoustic impedances are $Z = 1.62\,MRayl$ and $Z_d = 25.0\,MRayl$, thus 15.4 times higher than acrylic and enough to efficiently emulate a fixed boundary condition

[18].

The acrylic samples are 8 mm thick and 250 mm wide and long enough so that end reflections do not affect measurements. Wall thinning was machined into two samples with $d_T = d_B = 2\,mm$, across the width of the sample. One sample was left with two machined surfaces free, creating discontinuity type (ii) shown in Fig.4(ii). In order to make a free-fixed discontinuity, type (iv), a 2 mm thick steel plate was prepared to fit one of the sides of the discontinuity void space. To ensure proper coupling, the steel plate was bonded with cyanoacrylate adhesive.

SH waves were generated and received using Periodic Permanent Magnet (PPM) Electromagnetic Acoustic Transducers (EMAT) from Sonemat Ltd with 10 mm nominal wavelength and 3 cycles of magnets. Thin aluminium foil self-adhesive tapes were applied at the generating and receiving positions to allow EMATs to generate and receive ultrasonic waves on a non-metallic sample. A RITEC® RPR-4000 Pulser/Receiver was used to generate and receive the signals from PPM EMATs. The received signal was acquired by an oscilloscope that was connected to a PC to automate data acquisition. The discontinuity position is at $x = 100\,mm$, being the origin defined at the position of the generating transducer. Receiving position is at $x = -172\,mm$, at the left of the transmitter and discontinuity. Since EMATs generate waves that propagate both forwards and backwards, this position allows reception of both incident and reflected waves. The excitation pulse was set to an 8 cycle tone burst at 137.3 kHz, the optimum operating frequency for generating the SH0 mode at 10 mm wavelength, considering the transverse wave speed of acrylic. This frequency corresponds to $\Omega = 1.6$, then $1 < \Omega < 2$ allowing mode conversion to the propagating SH1 mode (see Fig.2). Fig.11(a) shows the dimensional phase speed dispersion curves for an 8 mm thick acrylic plate. The nominal transducer wavelength line is shown by a dashed line, where one can see that it crosses the SH0 mode dispersion curve at the operating frequency. The spatial distribution of the EMAT and the exciting pulse define the transducer operating region [6, 17]. The operating region is also shown in Fig.11(a), where one can see that it is centred at the SH0 mode dispersion curve but is wide enough so it intersects the SH1 mode. Thus, the reflected SH1 mode due to mode conversion can also be detected. In order to ensure single-mode generation and separation of the converted

modes in reception, the dual excitation and reception on the upper and lower surfaces was adopted, following the procedure described in [23]. Fig.11(b) shows the experimental setup. This procedure ensures that symmetric and antisymmetric modes are separated. Since at the operating region there exist only the SH0 and SH1 modes, separation between symmetric and antisymmetric modes equals separation between these two SH modes.

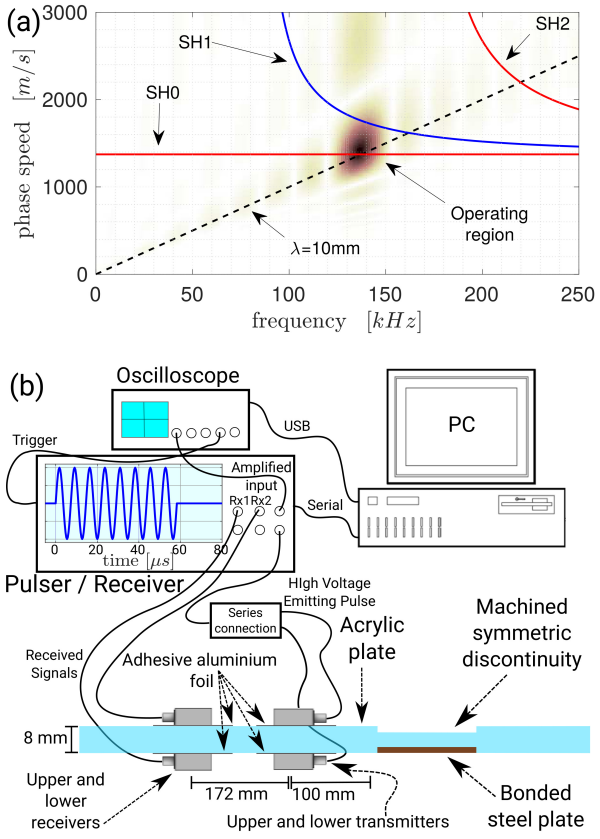

Figure 11: Experimental operating region (a) and setup (b). In (a), the phase speed dispersion curves of an 8 *mm* acrylic plate are shown together with the transducer nominal wavelength, dashed line, and operating region, behind the curves. In (b), the signal inside the illustrative pulser/receiver display is the driving current of 8 cycle tone-burst at 137.3 *kHz*.

Additional FEM simulations were performed to allow comparison with experimental signals. In this case, excitation was modelled differently than in the previous section, since it aims at approximately reproducing the experimental setup and the effect of the transducer. Therefore, generation was performed by imposing a 3 cycle spatial force distribution function with a period of 10 *mm*, similar to the spatial profile of the PPM

EMAT, on the surface nodes of the model, using a time history that was the same as the excitation current used in the experiment. This approach mimics the signal generated by a PPM EMAT without the need of including the EMAT coupling mechanism in the model, as validated previously elsewhere [6, 17, 23–25]. Similar to the experimental setup, numerical signals were mode-separated using the dual transduction procedure [23]. In order to consider the effect of the finite-size receiver, the numerical response field was further convolved with a 3 cycle spatial tone burst with 10 *mm* period to simulate the effect of the receiving transducer spatial profile on the acquired signals [6, 17].

It is worth highlighting that acrylic material imposes a much higher attenuation as usually found in metals, for instance. This requires extra attention when conducting the experiment since the amplitude of the received signal considerably reduces as the propagation distance increases. In order to overcome this, higher gain had to be used for detecting the reflected echoes, whose propagating path was longer. Besides, in order to calculate meaningful values for the reflection coefficients obtained in experiments and fairly compare them with numerical ones, in which damping was not included, attenuation has to be compensated in the experimental signals. This was performed by experimentally calculating the amplitude decay rate per propagated length measured at several positions in a non-machined plate. This attenuation coefficient is then used to post-compensate the amplitude of the experimental signals, considering the whole propagated distance at the receiving point. This procedure has been previously validated elsewhere [6, 17].

6.2. Experimental results

Fig.12(a) and (c) show the experimental and numerical received signals, respectively, for symmetric and antisymmetric modes when interacting with the symmetric discontinuity with both free surfaces, type (ii). Amplitude was normalized with respect to the received experimental direct pulse. The signal at around 150 μs corresponds to the generated pulse and the signals around 300 μs to the reflected wave from the discontinuity. As can be seen, there is a low-amplitude antisymmetric component around the generating signal, due to the inherent imprecision of the experimental mode selectivity procedure, which is higher for selecting modes with opposite symmetry to the generated one [23], and is also possibly due to slight differences in the boundaries where the aluminium tape

was applied in both plate's surfaces. The experimental reflected wave around 300 μs has a much lower amplitude than the numerically generated reflected wave result, due to the aforementioned high attenuation of acrylic. In order to obtain a higher signal level for the reflected mode, signals were reacquired with 20 dB more receiver gain, shown in Fig.12(b), whilst numerical signals, Fig.12(d), were normalized with respect to the experimental reflected pulse, so both show the same amplitude. It is worth noticing that this normalization is merely a graphical representation for easing comparison of the signals' shape; quantitative evaluation of the reflection magnitude was assessed by calculating the reflection coefficients, reported at the end of the section. As it can be seen, the symmetric discontinuity with both free boundary conditions produces uniquely symmetric reflected modes, due to the incident SH0 mode, as observed previously [17]. One can notice, however, a low-amplitude antisymmetric experimental signal due to mode separation imprecision and possibly, non-perfect symmetric machining.

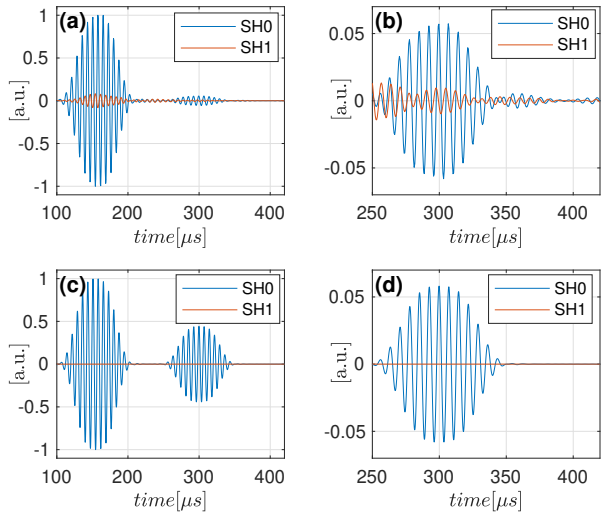

Figure 12: Experimental (a) and (b) and numerical (c) and (d) signals obtained due to the reflection of an incident SH0 mode at a symmetric discontinuity with both free surfaces, type (ii). Generated SH0 mode and reflected SH0 and SH1 modes, (a) and (c), normalized per incident wave. Detail of normalized reflected SH0 and SH1 modes acquired with 20 dB more gain, (b), and numerical signal normalized with respect to experimental one, (d).

Fig.13 shows the corresponding signals due to the interaction with symmetric discontinuity with opposite boundary condition. One can clearly see that the behaviour of the

reflected pulse is the opposite, i.e., the SH1 reflected mode is much more intense than the reflected SH0 mode. Experimental and numerical signals present a slight difference in their shapes. Some factors may contribute to it, such as, wavelength shift of converted modes [7] which mismatches the transducer nominal wavelength. As shown in Fig.11(a), at the operating frequency the SH1 mode does not cross the nominal wavelength line. This can cause some distortion on the converted-mode signal [23]. Others possible factors are imprecision on the transducers positioning on both surfaces of the plate or differences of adhesiveness of the applied aluminium foil on both surfaces, which introduces higher errors for separating converted modes than non-converted ones [23]; and also the effect of material attenuation, which introduces a frequency-dependent amplitude reduction factor for the travelling waves being an additional source for pulse distortion. Nevertheless, good agreement between simulation and experiment was achieved and the symmetry inversion behaviour was effectively observed experimentally.

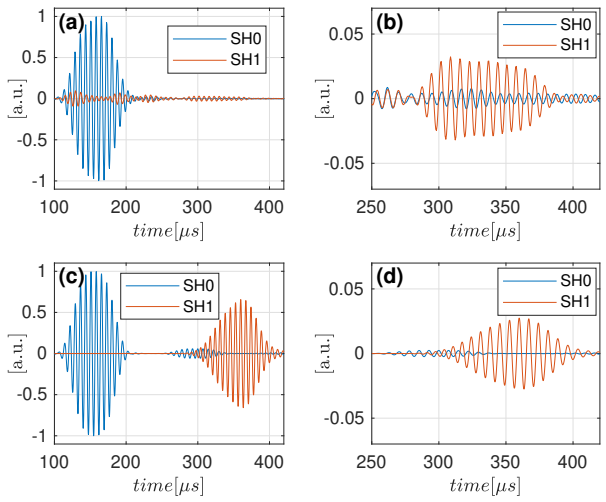

Figure 13: Experimental (a) and (b) and numerical (c) and (d) signals obtained due to the reflection of an incident SH0 mode at a symmetric discontinuity with opposite free and fixed boundary conditions, type (iv). Generated SH0 mode and reflected SH0 and SH1 modes, (a) and (c), normalized per incident wave. Detail of normalized reflected SH0 and SH1 modes acquired with 20 dB more gain, (b), and numerical signal normalized with respect to experimental one, (d).

Experimental reflection coefficients for converted and non-converted modes were calculated following Eq.39a, in which the peak-to-peak amplitudes were prior compensated

for attenuation, as explained above. The reflection coefficient is shown in Table 1 for experimental and corresponding numerical signals. As it can be seen, the symmetry inversion when interacting with a symmetric discontinuity with opposite boundary condition is experimentally proved. Good agreement between experimental and numerical coefficients was obtained.

Table 1: Experimental and numerical reflection coefficient due to the interaction of the SH0 with symmetric discontinuities types (ii) and (iv).

Disc. Type	(ii)		(iv)	
Conv. Mode	SH0	SH1	SH0	SH1
Exp.	0.426	0.084	0.077	0.573
Sim.	0.442	0.000	0.053	0.675

7. Conclusion

An analytical model to obtain the reflection and transmission coefficients due to the interaction of SH guided waves with discontinuities was devised based on the reciprocity principle. The model is able to solve discontinuities placed on one or both surfaces of the plate, being each side either free or fixed. It was used to investigate the interaction of guided SH wave modes with non-symmetric, symmetric and symmetric with opposite free-fixed boundary conditions, whose results agreed with numerical finite element analysis.

A symmetric discontinuity with the same boundary conditions on both surfaces restricts mode-conversion, preserving the incident mode symmetry, whereas it has been proved, for the first time, that when the boundary conditions are opposite it virtually restricts mode-conversion to modes with opposite symmetry as the incident one, behaving as a symmetry inverter discontinuity. This phenomenon depends on the frequency of the incident SH wave; the higher the frequency, the more effective symmetry inversion is. Similar reflection coefficients occur whether the fixed discontinuity is modelled only at its vertical wall or is completely fixed all along the discontinuity length.

The symmetry inversion phenomenon was experimentally verified by bonding a steel layer as a high acoustic impedance material in an acrylic plate which was symmetrically

machined.

Acknowledgments

This study was financed in part by the Coordenação de Aperfeioamento de Pessoal de Nível Superior - Brasil (CAPES) - Finance Code 001, and by the Brazilian National Council for Scientific and Technological Development, CNPq. The authors thank Marcio Coelho for technical support.

References

[1] A. Demma, P. Cawley, M. Lowe, Scattering of the fundamental shear horizontal mode from steps and notches in plates, J Acoust Soc Am 113 (4) (2003) 1880–1891.

[2] P. Rajagopal, M. J. S. Lowe, Scattering of the fundamental shear horizontal guided wave by a part-thickness crack in an isotropic plate, J Acoust Soc Am 124 (5) (2008) 2895–2904.

[3] S. Wang, S. Huang, W. Zhao, Z. Wei, 3D modeling of circumferential SH guided waves in pipeline for axial cracking detection in ili tools, Ultrasonics 56 (C) (2015) 325 – 331.

[4] M. Clough, M. Fleming, S. Dixon, Circumferential guided wave EMAT system for pipeline screening using shear horizontal ultrasound, NDT & E Int. 86 (2017) 20 – 27.

[5] J. Combaniere, P. Cawley, K. McAughey, J. Giese, Interaction between SH0 guided waves and tilted surface-breaking cracks in plates, IEEE Trans. on Ultrasonics, Ferroelectrics, and Frequency Control 66 (1) (2019) 119–128.

[6] A. C. Kubrusly, M. A. Freitas, J. P. von der Weid, S. Dixon, Interaction of SH guided waves with wall thinning, NDT & E Int. 101 (2019) 94 – 103.

[7] Nurmalia, N. Nakamura, H. Ogi, M. Hirao, K. Nakahata, Mode conversion behavior of SH guided wave in a tapered plate, NDT & E Int. 45 (1) (2012) 156 – 161.

[8] A. Pau, D. V. Achillopoulou, F. Vestroni, Scattering of guided shear waves in plates with discontinuities, NDT & E Int. 84 (C) (2016) 67 – 75.

[9] A. Pau, D. V. Achillopoulou, Interaction of shear and rayleighlamb waves with notches and voids in plate waveguides, Materials 841 (10.7) (2017) 3–14.

[10] Nurmalia, N. Nakamura, H. Ogi, M. Hirao, Mode conversion and total reflection of torsional waves for pipe inspection, Japanese Journal of Applied Physics 52 (7S) (2013) 07HC14.

[11] A. Pau, D. Capecchi, F. Vestroni, Reciprocity principle for scattered fields from discontinuities in waveguides, Ultrasonics 55 (2015) 85 – 91.

[12] J. Lee, J. D. Achenbach, Y. Cho, Use of the reciprocity theorem for a closed form solution of scattering of the lowest axially symmetric torsional wave mode by a defect in a pipe, Ultrasonics 84 (2018) 45 – 52.

[13] B. Poddar, V. Giurgiutiu, Scattering of Lamb waves from a discontinuity: An improved analytical approach, Wave Motion 65 (2016) 79 – 91.

[14] J. J. Ditri, Some results on the scattering of guided elastic sh waves from material and geometric waveguide discontinuities, J Acoust Soc Am 100 (5) (1996) 3078–3087.

[15] M. Koshiba, K. Hasegawa, M. Suzuki, Finite-element solution of horizontally polarized shear wave scattering in an elastic plate, IEEE Trans. on Ultrasonics, Ferroelectrics, and Frequency Control 34 (4) (1987) 461–466.

[16] J. D. Achenbach, Reciprocity in Elastodynamics, Cambridge Monographs on Mechanics, Cambridge University Press, 2004.

[17] A. C. Kubrusly, J. P. von der Weid, S. Dixon, Experimental and numerical investigation of the interaction of the first four SH guided wave modes with symmetric and non-symmetric discontinuities in plates, NDT & E Int. 108 (2019) 102175.

[18] A. C. Kubrusly, P. Tovar, J. P. von der Weid, S. Dixon, Numerical investigation of mode conversion of SH guided waves in plates reflected from discontinuities with different symmetries, in: 2019 IEEE International Ultrasonics Symposium (IUS), 2019, pp. 2202–2205.

[19] J. L. Rose, Ultrasonic Guided waves in solid media, Cambridge University Press, 2014.

[20] X. Yan, F.-G. Yuan, A semi-analytical approach for SH guided wave mode conversion from evanescent into propagating, Ultrasonics 84 (2018) 430 – 437.

[21] G. Shkerdin, C. Glorieux, Lamb mode conversion in a plate with a delamination, J Acoust Soc Am 116 (4) (2004) 2089–2100.

[22] L. Moreau, M. Castaings, B. Hosten, M. V. Predoi, An orthogonality relation-based technique for post-processing finite element predictions of waves scattering in solid waveguides, J Acoust Soc Am 120 (2) (2006) 611–620.

[23] A. C. Kubrusly, M. A. Freitas, J. P. von der Weid, S. Dixon, Mode selectivity of SH guided waves by dual excitation and reception applied to mode conversion analysis, IEEE Trans. on Ultrasonics, Ferroelectrics, and Frequency Control 65 (7) (2018) 1239–1249.

[24] P. A. Petcher, S. Dixon, Mode mixing in shear horizontal ultrasonic guided waves, Nondestructive Testing and Evaluation (2016) 1–20.

[25] P. Petcher, S. Burrows, S. Dixon, Shear horizontal (SH) ultrasound wave propagation around smooth corners, Ultrasonics 54 (4) (2014) 997 – 1004.